Influence of the vortical wake behind wind turbines using a coupled Navier-Stokes/Vortex-Panel methodology

Sven Schmitz*, Jean-Jacques Chattot

Mechanical and Aeronautical Engineering, University of California Davis, One Shields Avenue, Davis, CA 95616, USA

Abstract

The present paper introduces a parallelized coupled Navier-Stokes/Vortex-Panel solver (PCS) for incompressible high Reynolds number flow around horizontal axis wind turbines (HAWT). This coupling methodology reduces both artificial dissipation and computational cost. The coupled solver is applied to the NREL Phase VI rotor for fully attached flow. Results obtained for local blade loads are compared with experimental data and a vortex model based on a Lifting Line approach (VLM). It is indeed found that local blade loads obtained depend on at least ten revolutions of the vortex sheet in the wake.

Keywords: Navier-Stokes; CFX; Vortex method; Coupling; Wind turbine; Numerical diffusion; NREL Phase VI rotor

1. Introduction

Artificial viscosity, which is necessary for the stability of Navier-Stokes solvers, is responsible for rapid numerical diffusion of vortical structures such as tip vortices and vortex sheets behind wind turbines after only 1–2 blade revolutions. The use of high-order discretization schemes combined with extensive grid refinement or vorticity confinement due to Steinhoff [1] are two common approaches to reduce numerical diffusion, yet computationally very expensive. The importance of maintaining vortical structures far into the wake is revealed in Fig. 1(a), showing a photograph of the NREL Phase VI rotor taken in the NASA Ames wind tunnel. For incompressible high Reynolds number flows, the convection of shed vorticity to the far-field is best carried out by a vortex method being entirely dissipation free and numerically very efficient. However, a vortex method such as [2] cannot predict complex 3D viscous flow phenomena particularly when separated flow occurs near the tip or the root of the blade. Aiming at both reducing numerical diffusion and computational cost while modeling correctly the flow physics, a novel approach has been developed in which the flow domain is split into near-field and far-field respectively. While the near-field is predicted by a commercially available Navier-Stokes solver, CFX 5.6, the far-field is represented by an in-house developed Vortex-Panel method, see Fig. 1(b) and (c).

2. Numerical methods

2.1. Coupling methodology

The Vortex-Panel method provides cartesian velocity components at each point C on the outer surface of the Navier-Stokes zone, which serve as boundary conditions for the Navier-Stokes solver. Several velocities are superimposed to contribute to the velocity at point C:

$$\mathbf{v_C} = \mathbf{v_{Wind}} + \mathbf{v_{Rot}} + \mathbf{v_{Body}} + \mathbf{v_{Vortex}} \quad (1)$$

with $\mathbf{v_{Wind}}$ being the incoming wind velocity, $\mathbf{v_{Rot}}$ the blade rotation entrainment velocity, $\mathbf{v_{Body}}$ the perturbation velocity due to the thickness of the rotor blade obtained from a chordwise distribution of sources and sinks, and $\mathbf{v_{Vortex}}$ the perturbation velocity due to a bound vortex and the trailing vortex sheet for a two-bladed rotor. Initially, $\mathbf{v_{Vortex}}$ is obtained from a Lifting Line model [2]. After a few time steps of the Navier-Stokes solver, the spanwise distribution of circulation Γ_j along the blade is determined by performing a velocity contour integral

* Corresponding author: Tel.: +1 (530) 754 7578; Fax: +1 (530) 752 4158; E-mail: shschmitz@ucdavis.edu

Computational Fluid and Solid Mechanics 2005
K.J. Bathe (Editor)

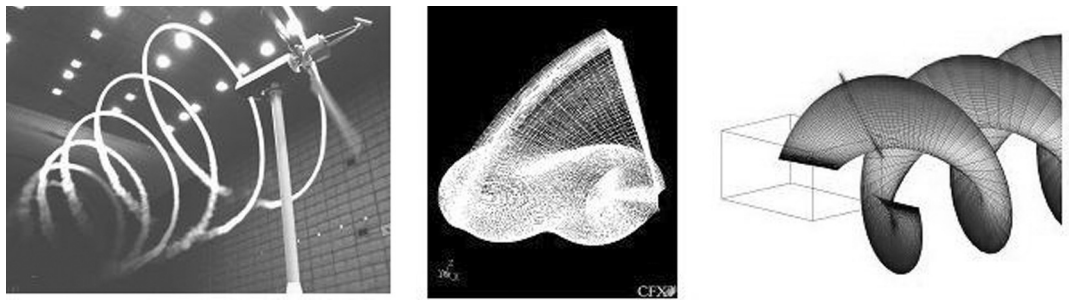

Fig. 1. Decomposition into near-field and far-field. (a) NREL Phase VI rotor; (b) Navier-Stokes zone; (c) Vortex-Panel method.

$$\Gamma_j = \oint_{L_j} \mathbf{v} \cdot \mathbf{ds} = \iint_{A_j} \omega \cdot \mathbf{dA} \tag{2}$$

where L_j is a closed contour around a radial section of blade and passes through the trailing edge. Stokes' theorem in Eq. (2) reveals that L_j has to be sufficiently large to include all sources of vorticity, namely the boundary layer. The distribution of circulation Γ_j serves as input for the Vortex-Panel method described in Section 2.3, which in turn provides an updated set of boundary conditions for the Navier-Stokes solver through Eq. (1). Coupling is performed after each 10–20 time steps of the Navier-Stokes solver until convergence is achieved for Γ_j with a threshold $\varepsilon = 10^{-5}$.

2.2. Navier-Stokes zone

The Navier-Stokes zone consists of a hybrid mesh with prisms and hexahedrons. The hybrid mesh contains a total of approximately 800,000 nodes, the rotor blade being meshed with 60 points along its local chord and 40 points in the spanwise direction. Prisms are extruded from the blade tips, while hexahedrons form a C-type mesh of 50 layers around one blade, its extruded tips, and a wake plane. Approximately 15 layers lie inside the boundary layer. The wake plane coincides with the first 60 degrees of the vortex helix generated by the vortex model, see Section 2.3, such that vortex filaments in Fig. 1(c) pass between nodes. This ensures that nodes are not located too close to vortex filament singularities. The flow is assumed to be steady and fully turbulent. The 3D incompressible Navier-Stokes equations are solved inside this zone using the k-ω two-equation turbulence model. Near-wall treatment is handled by scalable wall functions. The solver is parallelized on a cluster of four processors using the algorithm MeTis by Karypis et al. [3] for partitioning.

2.3. Vortex-Panel Method

Vortex sheet geometry

The vortex sheet consists of a bound vortex of variable strength, which lies on the y-axis coinciding with the blade's quarter chord, and a total of $jx = 41$ vortex filaments originating from the blade's trailing edge. Each vortex filament is divided into ix discrete pieces of non-uniform length, see Fig. 1(c). The vortex sheet is described in a rotating frame of reference using polar coordinates. Thus, the location of each discrete piece of vortex filament becomes

$$\begin{aligned} x_{i,j} &= x_{TE,j} + x_i \\ y_{i,j} &= r_j \cdot \cos(x_i/adv_i + \varphi_j) \\ z_{i,j} &= r_j \cdot \sin(x_i/adv_i + \varphi_j) \end{aligned} \tag{3}$$

where r_j and φ_j are the radius and phase angle of the trailing edge in the (x, y) plane. In Eq. (3), $adv_i = (V_{Wind} + u_i(x_i))/(\Omega * R)$ is defined as the advance ratio with V_{Wind} being the wind speed, Ω the angular rotor speed, and R the blade radius. A wind turbine extracts energy from the main flow and thus the vortex sheet will contract. The advance ratio at the blade $adv_T = (V_{Wind} + u_T)/(\Omega * R)$ is obtained by a power estimate prior to the run via $P = 2\pi\rho R^2(V_{Wind} + u_B)^2 u_B$. The advance ratio at the Trefftz plane $adv_T = (V_{Wind} + u_T)/(\Omega * R)$ is obtained using $u_B = 0.5 * u_T < 0$ from rotor disc theory and is achieved approximately four revolutions downstream of the rotor blade. It is the first approximately 60 degrees of the vortex sheet described in Eq. (3) that define the wake plane for the Navier-Stokes zone.

Biot-Savart law

Induced velocities due to the bound vortex and helicoidal vortex sheet are obtained from the Biot-Savart law

$$\mathbf{v}_{Vortex} = (u_{Vortex}, v_{Vortex}, w_{Vortex})^T = \int_{Vortex} \frac{\Gamma}{4\pi} \cdot \frac{\Delta\mathbf{l} \times \mathbf{r}}{r^3} \tag{4}$$

in discrete form with $\Delta\mathbf{l} = (\Delta x_{i,j}, \Delta y_{i,j}, \Delta z_{i,j})^T$ being a piece of vortex filament described by Eq. (3) and $\mathbf{r} = (x_C - x_{i,j}, y_C - y_{i,j}, z_C - z_{i,j})^T$ being the distance of that piece of vortex filament to an arbitrary point C on the boundary of the Navier-Stokes zone. The Cartesian velocity components in Eq. (4) are divided into contributions from the bound vortex and helicoidal trailing vortex filaments as

$$\begin{aligned} u_{Vortex} &= \frac{1}{4\pi}\sum_{j=1}^{jx} \delta\Gamma_j \cdot \left(a_j^{helix} + a_{j,rem}^{helix}\right) + \bar{\Gamma}_j \cdot a_j^{bound} \\ v_{Vortex} &= \frac{1}{4\pi}\sum_{j=1}^{jx} \delta\Gamma_j \cdot \left(b_j^{helix} + b_{j,rem}^{helix}\right) \\ w_{Vortex} &= \frac{1}{4\pi}\sum_{j=1}^{jx} \delta\Gamma_j \cdot \left(c_j^{helix} + c_{j,rem}^{helix}\right) + \bar{\Gamma}_j \cdot c_j^{bound} \end{aligned} \tag{5}$$

where the subscript j denotes the spanwise location on the blade and a, b, c are geometric influence coefficients for a two-bladed rotor. These coefficients have to be computed for each bound vortex and helicoidal vortex

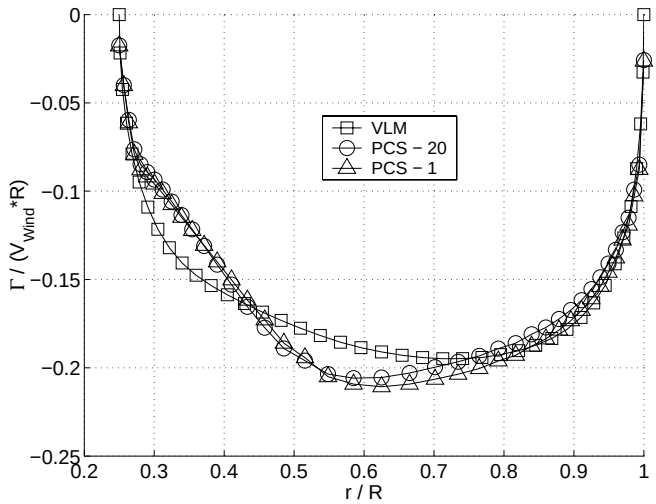

Fig. 2. Spanwise distribution of circulation ($V_{Wind} = 7$ m/s).

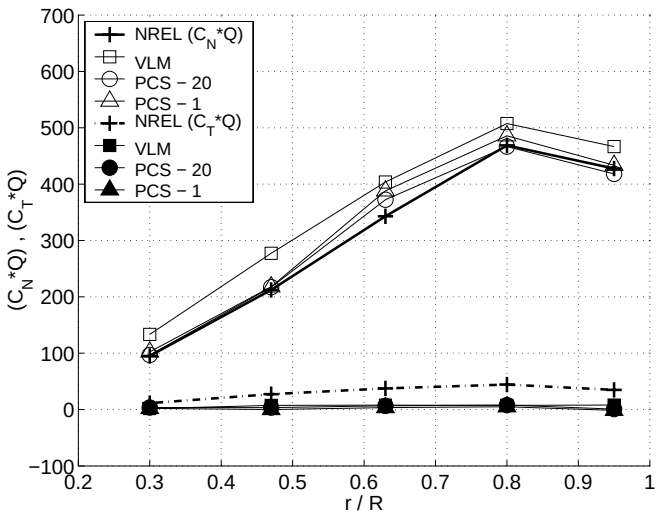

Fig. 3. Local normal and tangential forces ($V_{Wind} = 7$ m/s).

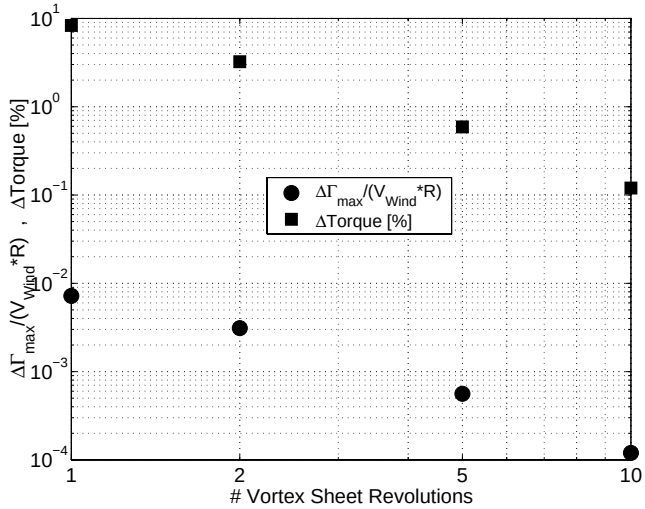

Fig. 4. Influence of the number of vortex sheet revolutions modeled.

filament at each point C on the boundary of the Navier-Stokes zone by using a discrete form of the Biot-Savart law in Eq. (4). In Eq. (5), the subscript *rem* denotes remainder terms, which are obtained by substituting Eq. (3) for large values of x_i into the Biot-Savart law and performing an asymptotic estimate of the general integral. The asymptotic estimate starts 20 revolutions of the vortex sheet behind the blade. A detailed derivation of the influence coefficients in Eq. (5) can be found in [4].

3. Results

The PCS solver has been applied to the NREL Phase VI Rotor configuration, see [5], for a wind speed of $V_{Wind} = 7\,\mathrm{m/s}$ where the flow is fully attached along the entire span. Local Reynolds numbers range from $5.8 \times 10^5 - 9.5 \times 10^5$, local Mach numbers are less than 0.12. The spanwise distribution of circulation is shown in Fig. 2 for VLM and two PCS runs considering 1 and 20 revolutions of the vortex sheet, PCS-1 and PCS-20. Differences between PCS and VLM are apparent and attributed to the fact that the VLM model in [2] does not account for 3D effects along the blade. Figure 2 also illustrates the influence of the vortical wake for $r/R > 0.55$. Results for PCS-20 show good agreement with experimental data from NREL [5] for the normal forces in Fig. 3, revealing once more that maintaining the vortex sheet far into the wake is essential for modeling correctly the flow physics, see Fig. 1(a). Discrepancies between experimental and numerical data for the tangential forces are attributed to the fact that fully turbulent flow was assumed, while experiments showed transitional. The influence of the number of vortex sheet revolutions on the circulation distribution and the integrated rotor torque is shown in Fig. 4. The reference case for the comparison is PCS-20. It can be seen that rotor torque differs by approximately 8% for PCS-1 and 3% for PCS-2 revealing that capturing the vortex sheet for only 1–2 revolutions is not sufficient for accurate prediction of rotor torque. On the other hand, rotor torque changes only by approximately 0.1% from PCS-10 to PCS-20.

4. Conclusions

A commercially available Navier-Stokes solver, CFX 5.6, has been coupled with an in-house developed Vortex-Panel Method for the numerical analysis of wind turbines. Results show good agreement with experimental data and the effect of the vortical wake on the solution has been studied. The main advantage of the presented methodology is the small size of the Navier-Stokes zone equipped with a grid that captures the vortex sheet in the best possible way. This reduces computational cost to a fraction of a full domain Navier-Stokes analysis. The vortex sheet is maintained far into the wake with very little dissipation using the Vortex-Panel Method.

References

[1] Steinhoff J, Underhill D. Modification of the Euler equations for vorticity confinement: application to the computation of interacting vortex rings. Phys Fluids 1994;6:2738–2744.

[2] Chattot JJ. Design and analysis of wind turbines using helicoidal vortex model. J Comput Fluid Mech 2002;11(1):50–54.
[3] Karypis G, Kumar V. Parallel multilevel k-way partitioning scheme for irregular graphs. Technical Report 036, University of Minnesota, 1996.
[4] Schmitz S, Chattot JJ. A coupled Navier-Stokes/vortex-panel solver for the numerical analysis of wind turbines. Proc of the ICCFD3, Toronto, July 2004.
[5] Fingersh LJ, Simms D, Hand M, Jager D, Cotrell J, Robinson M, Schreck S, Larwood S. Wind tunnel testing of NREL's unsteady aerodynamics experiment. AIAA-2001-0035, pp. 194–200.